Bioactive Materials 17 (2022) 261–275

Contents lists available at ScienceDirect

Bioactive Materials

journal homepage: www.keaipublishing.com/en/journals/bioactive-materials

Fabrication of channeled scaffolds through polyelectrolyte complex (PEC) printed sacrificial templates for tissue formation

Haoyu Wang [a,b], Xiaqing Zhou [a,b], Juan Wang [a], Xinping Zhang [d], Meifeng Zhu [a,c,**], Hongjun Wang [a,b,*]

[a] Department of Biomedical Engineering, Stevens Institute of Technology, Hoboken, NJ, 07030, United States
[b] Department of Chemistry and Chemical Biology, Stevens Institute of Technology, Hoboken, NJ, 07030, United States
[c] College of Life Science, Key Laboratory of Bioactive Materials, State Key Laboratory of Medicinal Chemical Biology, Xu Rongxiang Regeneration Life Science Center, Nankai University, 300071, Tianjin, PR China
[d] School of Medicine and Dentistry, University of Rochester Medical Center, Rochester, NY, 14642, United States

ARTICLE INFO

Keywords:
Embedded 3D printing
Porous channeled scaffold
Scalable 3D framework
Polyelectrolyte complex

ABSTRACT

One of the pivotal factors that limit the clinical translation of tissue engineering is the inability to create large volume and complex three-dimensional (3D) tissues, mainly due to the lack of long-range mass transport with many current scaffolds. Here we present a simple yet robust sacrificial strategy to create hierarchical and perfusable microchannel networks within versatile scaffolds via the combination of embedded 3D printing (EB3DP), tunable polyelectrolyte complexes (PEC), and casting methods. The sacrificial templates of PEC filaments (diameter from 120 to 500 μm) with arbitrary 3D configurations were fabricated by EB3DP and then incorporated into various castable matrices (e.g., hydrogels, organic solutions, meltable polymers, etc.). Rapid dissolution of PEC templates within a 2.00 M potassium bromide aqueous solution led to the high fidelity formation of interconnected channels for free mass exchange. The efficacy of such channeled scaffolds for in vitro tissue formation was demonstrated with mouse fibroblasts, showing continuous cell proliferation and ECM deposition. Subcutaneous implantation of channeled silk fibroin (SF) scaffolds with a porosity of 76% could lead to tissue ingrowth as high as 53% in contrast to 5% for those non-channeled controls after 4 weeks. Both histological and immunofluorescence analyses demonstrated that such channeled scaffolds promoted cellularization, vascularization, and host integration along with immunoregulation.

1. Introduction

Scaffold-guided tissue formation remains the mainstream for in vitro creation of tissue-engineered constructs or in vivo regeneration of diseased or damaged tissues [1]. Typically, the scaffolds made from different materials would define a regulatory microenvironment to the resident cells with instructive cues. Oftentimes it is also preferable for such scaffolds to have an interconnected channel network with desirable channel size, well-designed hierarchical architectures, and optimized compartmentalization, allowing not only for controllable cellular activities (e.g., attachment, migration, and differentiation) but also for adequate nutrient supplies and tissue ingrowth during new tissue formation [2,3].

Increasing evidence has demonstrated that incorporating the structural complexity in scaffold design can better mimic the unique mechanical and biological functions of native tissue extracellular matrix (ECM) and subsequently guide the directional and spatial formation of preferred tissue structures, such as vasculature and neuronal networks. As such, extensive endeavors are committed to developing various hierarchical structures using particulate leaching [4,5], gas-foaming [6], lyophilization [7], and three-dimensional (3D) printing [8–10]. In particular, 3D printing, a computer-aided technique, exhibits the capability of reproducibly and readily customizing complex 3D geometries with well-controlled micro-and macro-structures while overcoming

Peer review under responsibility of KeAi Communications Co., Ltd.
* Corresponding author. Department of Biomedical Engineering, Stevens Institute of Technology, Hoboken, NJ, 07030, United States.
** Corresponding author. College of Life Science, Key Laboratory of Bioactive Materials, State Key Laboratory of Medicinal Chemical Biology, Xu Rongxiang Regeneration Life Science Center, Nankai University, 300071, Tianjin, PR China.
E-mail addresses: zhumeifeng@nankai.edu.cn (M. Zhu), hongjun.wang@stevens.edu (H. Wang).

https://doi.org/10.1016/j.bioactmat.2022.01.030
Received 18 November 2021; Received in revised form 15 January 2022; Accepted 18 January 2022
Available online 29 January 2022
2452-199X/© 2022 The Authors. Publishing services by Elsevier B.V. on behalf of KeAi Communications Co. Ltd. This is an open access article under the CC BY-NC-ND license (http://creativecommons.org/licenses/by-nc-nd/4.0/).

Table 1
Comparison of sacrificial template materials used for creating channeled scaffolds from castable materials.

		Sacrificial Template Materials				
		Hydrogel [28]	Sugar [24]	Photosensitive materials [32,33]	Polymer [22,23,34]	PEC
Applicability	Thermal sensitive materials					✓
	UV cross-linkable materials	✓	✓	✓		✓
	pH-sensitive materials	✓	✓			✓
	Solvent evaporable materials				✓	✓
Cost		Moderate	Low	High	Moderate	Low
Printability		Low	Moderate	High	Moderate	High
Recyclability		No	No	No	No	Yes

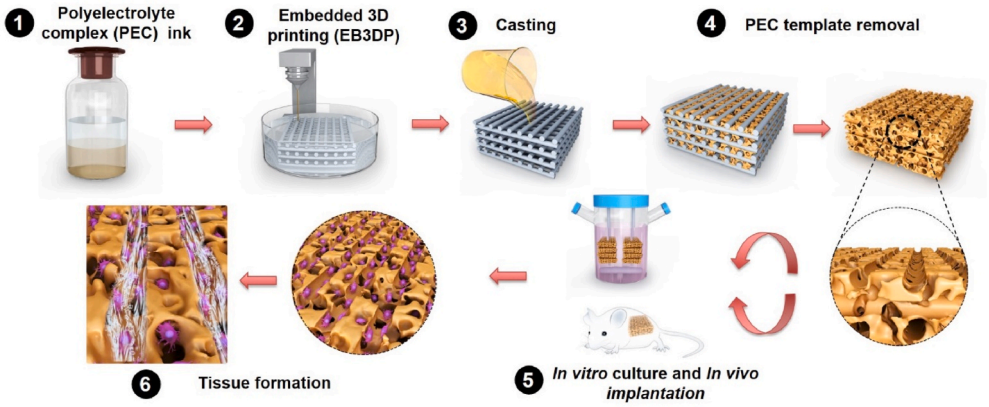

Fig. 1. A diagrammatic illustration of the key procedures involved in the formation of versatile channeled scaffolds with 3D hierarchical, arbitrary, and patent luminal networks through a 3D printed sacrificial polyelectrolyte complex (PEC) template-aided strategy.

apparent limitations with other fabrication technologies, such as unpredictable spatial organization and the lack of interconnected channels for tissue ingrowth and free mass exchange. Along with a successful demonstration of its application potentials with diverse materials, however, such printed ECM-like analogs often fail to recapitulate the unique bio-fidelity and cellular complexity of their natural counterparts, partly owing to the limited printing resolution, which is closely regulated by the motion path of the printing head, printing nozzle size, and subsequent high-pressure resistance [7,11]. Although stereolithography-based 3D printing could reach a high printing resolution, it is solely applicable to those photocrosslinkable materials with constraint adaptability [12,13]. On the other hand, bioprinting, a process of fabricating 3D tissue constructs from cell-laden bioinks, enables the spatiotemporally controlled organization of cells and biomolecules to fabricate complex and biomimetic tissue constructs. However, the current bioprinted tissue constructs are not ready to scale up for large or oriented tissue formation [14]. In particular, the lack of channel networks throughout 3D tissue constructs leads to inadequate interior supplies of oxygen and nutrients for in vitro tissue development, and causes the poor mass distribution to impede effective integration with the host upon in vivo implantation [15]. Cumulative evidence also highlights the regulatory roles of the interconnected channel structures to the cells in terms of controlled adhesion, directed migration, and regulated phenotype [16–18].

In view of the essence of channeled networks in tissue regeneration, efforts are accordingly made to create open channels within various scaffolds [19–21]. Apart from direct printing of selected materials (e.g., polycaprolactone (PCL), gelatin methacryloyl (GelMA), alginate hydrogel) into channeled scaffolds via additive manufacturing, particular interests are also geared toward the utilization of sacrificial templates as a reverse casting mold to develop perfusable and hierarchical microchannel networks [22,23] (Table 1). One exemplar effort from Miller et al. is the use of printed carbohydrate-glass sacrificial filaments to form microchannels within cell-laden gels [24]. In order to maintain the integrity of water-soluble carbohydrate-glass templates in a hydrogel-based cast, a multi-step polymer coating was essential to protect these templates from dissolution. In addition, several other associated challenges such as 'response lag' in material hardening and solidifying procedure and the fragility of printed structures that require an extra supporting interface and optimized printing path precision to minimize filament breakage and deformation restricted its comprehensive utility as a sacrificial template, especially in the fabrication of large volume and complex porous scaffolds. However, it evidently demonstrates the efficacy of printed sacrificial templates in creating open channels in hydrogel-based materials.

In many native tissues and organs, the presence of hierarchical and intricate network structures, i.e., vascular and neuronal networks, is essential to achieve unique physiological functions via closely interacting with surrounding stroma. To partially, if not fully recapitulate such networks, the creation of versatile and arbitrary 3D channel structures within engineered scaffolds would be an effective avenue to guide the regeneration of such network systems. In this regard, it is highly desirable to establish an enabling platform allowing to print the sacrificial templates with arbitrary configurations. Embedded 3D printing (EB3DP) [25], an emerging technology offering omnidirectional free-form fabrication within a soft substrate to support the patterned material, could potentially endow more complexities and controllability to the printed sacrificial templates [26]. To enable the EB3DP, both viscoelastic ink and supporting matrix need to meet several key criteria, including the shear-thinning property, an appropriate range of shear elastic modulus, and yield stress between the ink and matrix, and so on [27]. Recently, Wu et al. demonstrated the possibility of creating a 3D biomimetic microvascular-like network within UV cross-linked hydrogel matrix by printing a fugitive organic ink into designed patterns inside a photopolymerizable hydrogel matrix and then removing the fugitive template after UV cross-linking of the hydrogel [28]. However, the stringent experimental setup, limited options of UV-crosslinkable capabilities, and exclusive hydrogel-based platform

may significantly compromise the potentials of EB3DP. Moreover, a major practical challenge is the lack of a stable ink and supporting matrix couple with a high degree of freedom, a low barrier for processing, and a high error tolerance during printing.

To address the aforementioned challenges along with the intention to develop a widely applicable methodology, the overall objective of this study was to explore the use of polyelectrolyte complexes (PEC), an association complex of oppositely charged polyions, as the viscoelastic printing ink for sacrificial templates to establish an innovative, simple, eco-friendly, recyclable and scalable platform that can be applied to versatile materials for fabricating scaffolds containing 3D hierarchical and arbitrary channel structures (Fig. 1). More specifically, the polyelectrolytes of poly(diallyldimethylammonium chloride) (PDADMAC) and poly(sodium 4-styrenesulfonate) (PSS) are considered as a promising PEC pair for their demonstrated attributes, such as stoichiometrical complexation, good complexation strength, prompt doping/undoping capacity, sensitive ionic strength-dependent association/dissociation, tolerability of high temperature (as high as 350 °C), relatively high stiffness (~10 MPa), and negligible cytotoxicity [29]. Taking advantage of the tunable viscoelasticity of PDADMAC/PSS PEC and the phase transition of aqueous Pluronic F127 solutions (triblock copolymer solutions, yielding a physical gel of micelles consistent of a hydrophobic core surrounded by hydrophilic corona above a critical micelle concentration (25% w/v) under ambient conditions [28,30]), PEC with desirable viscoelastic properties was printed into pre-designed 3D structures within the 'supporting matrix' of Pluronic F127 gel at room temperature using EB3DP. Modulation of the filament size, the inter-filament distance, and the filament overlay angles could lead to the structural complexity of printed 3D PEC structures. Thanks to their mechanical stability and structural integrity, the printed PEC structures could be easily extracted from Pluronic F127 upon liquifying Pluronic F127 at a lower temperature (e.g., 4 °C). The resulting PEC prints were then used as the sacrificial templates for a broad spectrum of castable materials (such as polymer melt, synthetic and natural polymer solutions, thermoresponsive hydrogel, and photocrosslinkable hydrogel) (Table 1) and maintained the structural integrity after solidification. As a result of the sensitive dissociation response of PEC to external stimuli such as pH and ionic concentration, the hierarchical PEC templates could be readily removed and leave opening channel networks inside the bulk materials for perfusion of nutrients and spatial guidance of tissue ingrowth [31]. Clearly, this study not only demonstrates the possibility of creating hierarchical channel networks within the scaffolds, but also offers an effective avenue to rapidly and reproducibly formulate versatile arbitrary patterns for the spatial organization of cells with anisotropy and complexity in tissue engineering and beyond.

2. Materials and methods

2.1. Materials

Poly(diallyldimethylammonium chloride) (PDADMAC, Mw = 150,000–200,000 Da), poly(sodium 4-styrenesulfonate) (PSS, Mw = 500,000 Da), potassium bromide (KBr, ≥ 99.0%), sodium chloride (NaCl, ≥ 99.0%), Pluronic® F127, 1,8-octane diol (98%, Mw = 146.23), citrate acid (99.5%, Mw = 210.14), agarose, gelatin-methacrylate (GelMA, TissueFab®), glutaraldehyde solution (25% in water), glycine (≥99.0%) chloroform (≥99.0%) and polystyrene (PS, Mw = 192,000 Da) were purchased from Sigma-Aldrich (St. Louis, MO). Collagen (Type I) was obtained from Elastin Products Inc. (Owensville, MO). 3-(4,5-dimethylthiazol-2-yl)-5-(3-carboxymethoxyphenyl)-2-(4-sulfophenyl)-2H-tetrazolium) (MTS) assay kit was purchased from Promega (Madison, WI) and fetal bovine serum (FBS) was obtained from Atlantic Biologicals (Atlanta, GA). All other reagents and solutions were from Thermo Fisher (Waltham, MA) unless otherwise indicated.

2.2. Preparation of PEC printing ink

The PEC printing inks were prepared by mixing PDADMAC and PSS at a concentration of 2.50 M with respect to their monomer units at a volume ratio of 1:1 in a beaker with deionized water and 0.25 M NaCl at room temperature. PEC precipitate was collected and then centrifuged using Eppendorf 5804R at 10,000 rpm for 15 min. All PEC precipitates were dried in the oven at 50 °C overnight. To identify the appropriate viscosity range of printable PEC solution, the dried PEC precipitates were respectively dissolved in 1.50 M, 1.65 M, 1.75 M, 1.85 M, and 2.00 M KBr aqueous solution for 12 h. Upon discarding the supernatants, the viscous PEC coacervates were collected and used for printing. To avoid the unwanted change of the rheological properties, the PEC coacervates were used within 24 h.

2.3. Rheological characterization

Rheological properties of PEC coacervates and Pluronic F127 were determined with an Advanced Rheometric Expansion System (ARES) rheometer (TA Instruments, New Castle, DE) with force rebalance transducer 2 KFRTN1 and stainless steel parallel disks. The actuator of the ARES is a dc servomotor, and its shaft is supported by an air bearing with an angular displacement range of 0.05–500 mrad. A resolution of 0.005 mrad can be achieved. All the tests were performed using rotational rheometry under hydrated conditions. The PEC immersed in the respective KBr solutions (1.50 M, 1.65 M, 1.75 M, 1.85 M, and 2.00 M) was kept at ambient temperature during rotational rheometry to prevent drying. The chamber holding the solution consisted of two concentric cylindrical dishes: one was sealed and attached to the lower fixture, which was connected to the torque and the standard force transducers, and another was attached to the upper fixture of the rheometer, which was coupled to the motor.

2.4. Printing of PEC

25% (w/v) pluronic F127 in deionized water was prepared and used as a supporting matrix for the collection bath. The matrix was settled in a customized plastic container at room temperature until the phase transition was fully accomplished (~10 min). Then the container was fixed on the stage of a customized 3D printer. The printable PEC coacervate was transferred to a 3-mL syringe and extruded through a 5-mm long, 26 G (inner diameter: 0.26 mm; outer diameter: 0.46 mm), tip-blunt nozzle (BD, Franklin Lakes, NJ) using an sp210c syringe pump (WPI, Sarasota, FL) with a tunable pumping rate from 0.1 mL h^{-1} to 1.2 mL h^{-1}. To form the designed structure, the printing head with free motion in X, Y, and Z directions were controlled by G-code that was programmed by AutoCAD 2015 software, manual coding using the open-source Slic3r software. The printed PEC structures were plasticized in the supporting matrix during printing. After printing, the collection container, together with the supporting matrix and printed PEC structures, were transferred to a 4 °C refrigerator until completely liquefying of the supporting matrix into a low-viscosity liquid (~10 min). Then the PEC prints were extracted and rinsed with deionized water 3 times prior to storage at 4 °C for further use.

2.5. Casting of multiple materials into PEC templates

2.5.1. Poly(1, 8 octanediol-co-citrate) (POC) cast

Anhydrous citric acid and 1,8-octane diol at an equal molar ratio were added into a 250-mL three-neck round-bottom flask and heated to 160–165 °C until a molten, clear mixture was formed by stirring. The temperature was then lowered to 140–145 °C for 1 h to form the prepolymer. The prepolymer was transferred into a customized Teflon mold containing the PEC printed templates and then post-polymerized at 100 °C for 1 day in a vacuum oven.

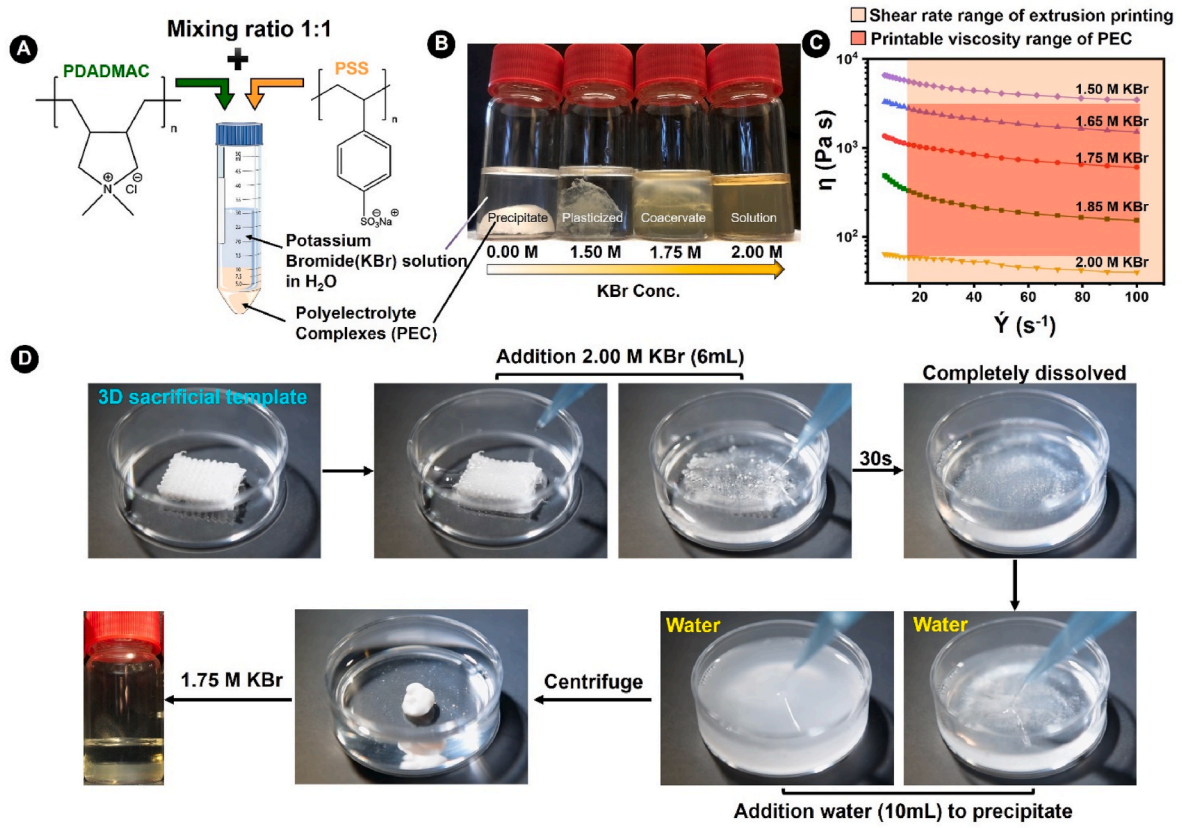

Fig. 2. Optimization of the key parameters relevant to the formulation of PEC printing inks and the recycling procedures of printed PEC templates. A) Schematic illustration on the preparation of PSS/PDADMAC PEC ink for EB3DP. B) Macroscopic images of the dissolution of PEC precipitates within different concentrations of KBr aqueous solutions. C) The viscosity flow curves of PEC dissolved in different concentrations of KBr solutions. D) Macroscopic visualization of the complete recycling procedures of 3D printed PEC templates.

2.5.2. Agarose cast

1% (w/v) agarose aqueous solution was prepared and heated up in a microwave oven for 30 s. The solution was cast onto the PEC printed template in a customized Teflon mold and then transferred into a 4 °C refrigerator for 10 min for complete solidification.

2.5.3. Collagen cast

Collagen gel solution was prepared by neutralizing collagen solution (3 mg mL^{-1} in 0.01 M HCl) with 5 × PBS, including 12.5 mg mL^{-1} sodium bicarbonate at a volume ratio of 4:1. The pH was adjusted to 7.4. After laying down a thin layer of collagen gel in the Teflon mold, the printed PEC templates were placed on top, followed by another layer of collagen gel to embed the PEC templates. Gelation was completed by incubation at 37 °C for 1 h.

2.5.4. Gelatin methacrylate (GelMA) cast

10% (w/v) GelMA prepolymer aqueous solution with 0.1% (w/v) photoinitiator (Irgacure 2959) was mixed and then poured into the Teflon mold containing the printed PEC templates. Gelation was completed by irradiating with ultraviolet (UV) light for 20 min. Later, the cast was cross-linked by the glutaraldehyde vapor from a 2.5% glutaraldehyde ethanol solution in a closed box at 37 °C for 8 h.

2.5.5. Polystyrene (PS) cast

8% (w/v) PS solution was prepared by dissolving PS granules in chloroform. The solution was continuously stirred overnight before casting and then poured into the Teflon mold with the printed PEC templates. The cast was left in the fume hood for 3 days for solvent evaporation.

2.5.6. Silk fibroin (SF) cast

40% (w/v) SF solution was prepared in the deionized water and then poured into the Teflon mold with printed PEC templates. After casting, the cast was then lyophilized for at least 12 h under a vacuum of 25 Pa. Afterward, the cast was cross-linked by the glutaraldehyde vapor from a 2.5% glutaraldehyde ethanol solution in a closed box at 37 °C for 8 h.

2.6. Removal of the PEC templates from various casts

All the casts of different materials were rinsed three times with 2.00 M KBr aqueous solution (10 min each time) to remove the PEC templates and then washed with a series of gradient KBr aqueous solutions (1.75 M, 1.50 M, 1.00 M) until pure deionized water. For GelMA and SF casts, additional steps were also taken after the PEC template removal. They were washed 5 times with cold deionized water (3 min each time) and then immersed in 0.1 M glycine aqueous solution for 12 h to block any unreacted aldehyde group. The scaffolds were further washed with deionized water 10 times (10 min each) prior to lyophilization.

2.7. Characterizations of channeled scaffolds

2.7.1. Stereomicroscope

The obtained scaffolds were examined with a Nikon SMZ1400 stereomicroscope (Nikon, Tokyo, Japan), and images were captured using NIS-ElementsBR 3.10 Software. The scaffolds were examined in two particular directions, i.e., parallel or perpendicular to the scaffold long axis. For the perfusion testing, the image capture rate was set as 1 frame per second.

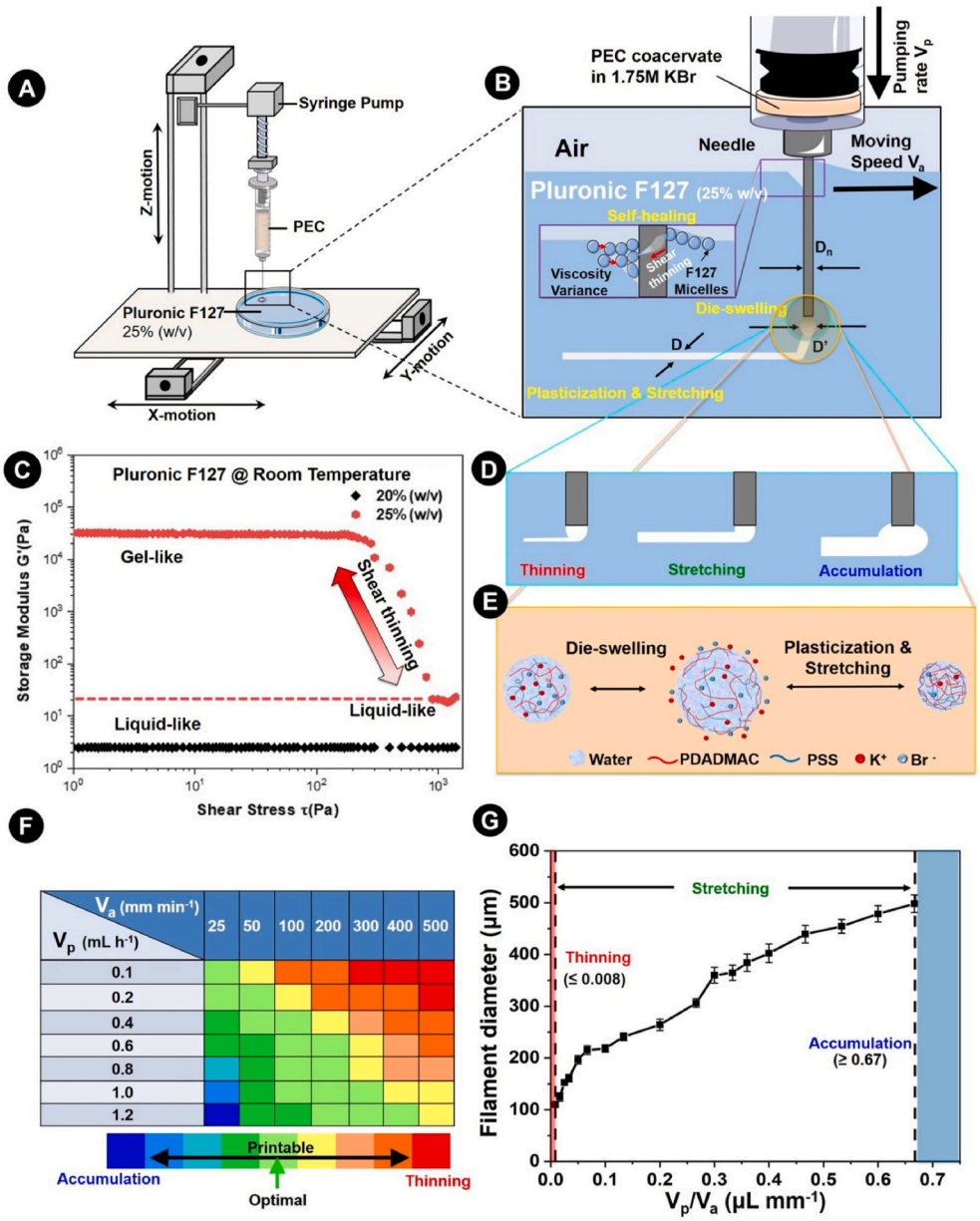

Fig. 3. Optimization of the key parameters relevant to the fabrication of PEC microfiber templates. A) Schematic illustration of the customized 3D printer and the setup for EB3DP. B) Schematic illustration of the key events during EB3DP. C) The rheological properties of two formulations of pluronic F127 at room temperature. D) Schematic illustration of three printing boundary conditions. E) Schematic elaboration on the rebalancing of counterions, water, and PEC pairs within 25% (w/v) aqueous pluronic F127 bath during the formation of PEC filaments. F) Color-coded map of the V_a and V_p in relation to the printability of PEC coacervate. G) Correlation between the filament diameter of 1.75 M KBr PEC coacervate and the value of V_p/V_a.

2.7.2. Scanning electron microscope

The scaffolds were sputter-coated with gold (1.5 nm thick), and micrographs were acquired with an Auriga Modular Cross Beam workstation (Carl Zeiss, Inc., Oberkochen, Germany) at 3.00 kV. Five randomly selected fields were obtained for each scaffold. Images were then analyzed using ImageJ software v1.5 (NIH, Maryland, US) to calculate the average microchannel diameter and pore size.

2.7.3. Micro-computed tomography (Micro-CT) evaluation

After tension-free drying, all scaffolds were subjected to the Micro-CT characterization. The analysis was conducted with a Micro-CT imaging system (SkyScan 1276, Allentown, PA, USA) using the scanning conditions: 50 kV, 70 mu A, no filter, with a spatial resolution of 3 μm. The obtained data were reconstructed by NRecon (Version: 1.7.1.6) software. Analysis of the region of interest (ROI) was selected by CTAn (Version: 1.17.9.0) software. Pore size and porosity were obtained along with the reconstruction of a 3D ROI map. CTvox (Version: 3.3.0.0) software was used for 3D image analysis and video generation.

2.7.4. Perfusion testing

Coomassie Brilliant Blue R purchased from Sigma-Aldrich (St. Louis, MO) was used as a blue dye for injection through the channels to evaluate the permeability. The dye solution was pumped into the scaffold from the opening at the bottom layer with an sp210c syringe pump (WPI, Sarasota, FL) at a flow rate of 2 mL h^{-1}. Both images and videos were recorded.

2.8. Dynamic seeding and culture of fibroblasts within channeled scaffolds

Mouse embryonic fibroblasts (STO, ATCC, VA) were cultured in Dulbecco's Modified Eagle's Medium (DMEM) supplemented with 2.2 g L^{-1} sodium bicarbonate, 20% FBS, and 1% penicillin-streptomycin. The culture was maintained at 37 °C with 5% CO_2 and 95% humidity until 70–80% confluence prior to use. To achieve homogeneous cell distribution within an individual scaffold and equally among multiple scaffolds, STO cells were seeded and cultured onto the scaffolds using a spinner flask [35,36]. Briefly, all scaffolds (8 mm × 8 mm × 2 mm) were

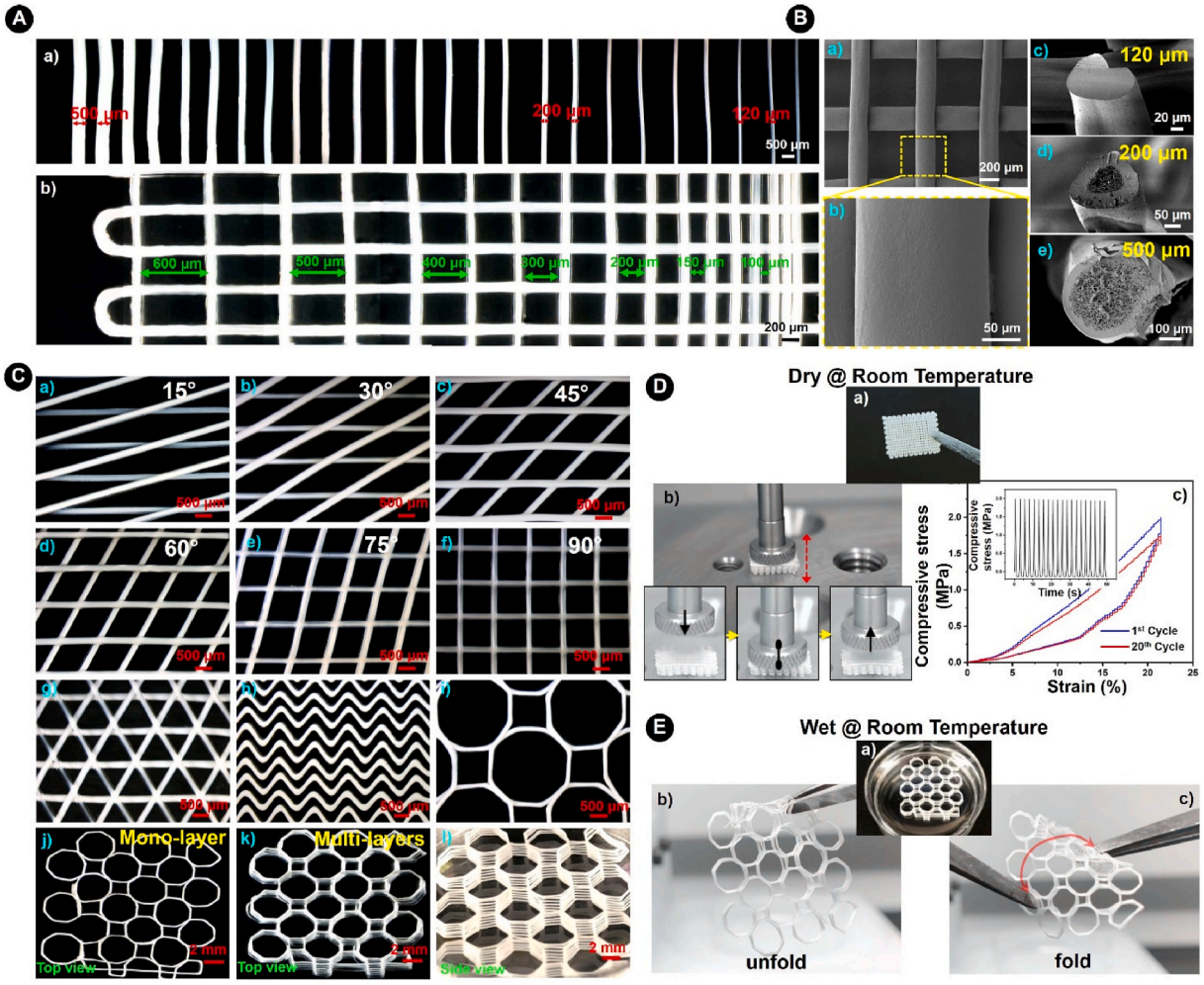

Fig. 4. Modulation of the spatial organization of PEC microfibers during EB3DP and the associated mechanical stabilities. A) Stereo microscopic images of various filament diameters and inter-filament distances. Scale bar: a) 500 μm; b) 200 μm. B) SEM micrographs of the PEC microfiber prints. L-a) Morphology of printed microfibers from 1.75 M KBr PEC coacervate, which has a relatively smooth surface upon zoomed-in examination (L-b). Cross-section of PEC filaments with the diameter of L-c)120 μm, L-d) 200 μm, and L-e) 500 μm from 1.75 M KBr PEC coacervate. Scale bar: a) 200 μm; b) 50 μm; c) 20 μm; d) 50 μm; e) 100 μm. C) Stereo microscopic images of the microfibers with different overlay angles from 15° to 90°, complex patterns, and multiple stacking layers. Scale bar: a-i) 500 μm; j-l) 2 mm. D) Characterization of PEC printed template at a dry condition. D-a) Macroscopic view of the dry PEC template. D-b) Macroscopic demonstrations on the mechanical stability of the dry PEC templates under a cyclic compression testing. D-c) The stress-strain curve of dry PEC templates after the 1st (blue) and 20th (red) compression cycle. E) Macroscopic view of wet PEC templates (a) without folding (b) and folding (c) to show the structural integrity.

sterilized with 70% ethanol and UV irradiation for 20 min on each side, and then the scaffolds were fixed inside a spinner flask (100 mL, Bellco Glass Inc., NJ). The STO cells suspensions (1.0×10^5 cells per scaffold) were added and stirred at 40 rpm using a 0.8 cm diameter × 4 cm long stir bar for 24 h. Afterward, the stirring speed was lowered to 20 rpm for continuous culture (7 days and 14 days).

2.9. Histological staining of in vitro tissue formation within channeled scaffolds

To better visualize the spatial distribution of newly formed tissue, the cultured constructs were fixed with 4% (w/v) paraformaldehyde (PFA) at 4 °C for 1 h after culture for 1 day, 7 days, and 14 days. Samples were rinsed gently three times with PBS and then immersed in 15% (w/v) and 30% (w/v) sucrose in PBS at 4 °C for 4 h, respectively. Then, all the samples embedded in an OCT freezing solution (Sakura Finetek, Tokyo, Japan) were frozen at −80 °C. The frozen samples were cut into thin sections (8 μm) using an HM 550 cryostat (Richard-Allan Scientific, Kalamazoo, MI) and collected on the HistoBond®+ adhesive glass slides (Marienfeld, Germany). The slides were fixed using cold acetone (−20 °C) for 3 min and left at room temperature overnight to dry prior to staining. The slides were then performed for hematoxylin and eosin (H&E) staining and Masson's trichrome staining. The stained slides were examined with a Nikon eclipse 80i epi-fluorescence microscope and images were accordingly recorded.

2.10. Cell proliferation

The adhesion (1 day) and proliferation (7 day and 14 day) of STO cells on the scaffolds were detected using the MTS assay. Briefly, the harvested culture constructs (n = 3) were placed in a 12-well plate and gently rinsed with cold PBS twice. Then 1.4 mL of a mixture containing 400 μL MTS reagent and 1 mL culture medium was added each well. The plate was incubated in 5% CO_2 at 37 °C for 2 h, and then 200 μL supernatant of each sample was transferred to a 96-well plate. The absorbance at 490 nm was recorded using the BioTek Synergy microplate reader (BioTek Instruments, Inc., Vermont, USA).

2.11. In vivo implantation of channeled scaffolds

The animal study was approved by the Animal Experiments Ethics Committee of Nankai University (Tianjin, China) in accordance with the

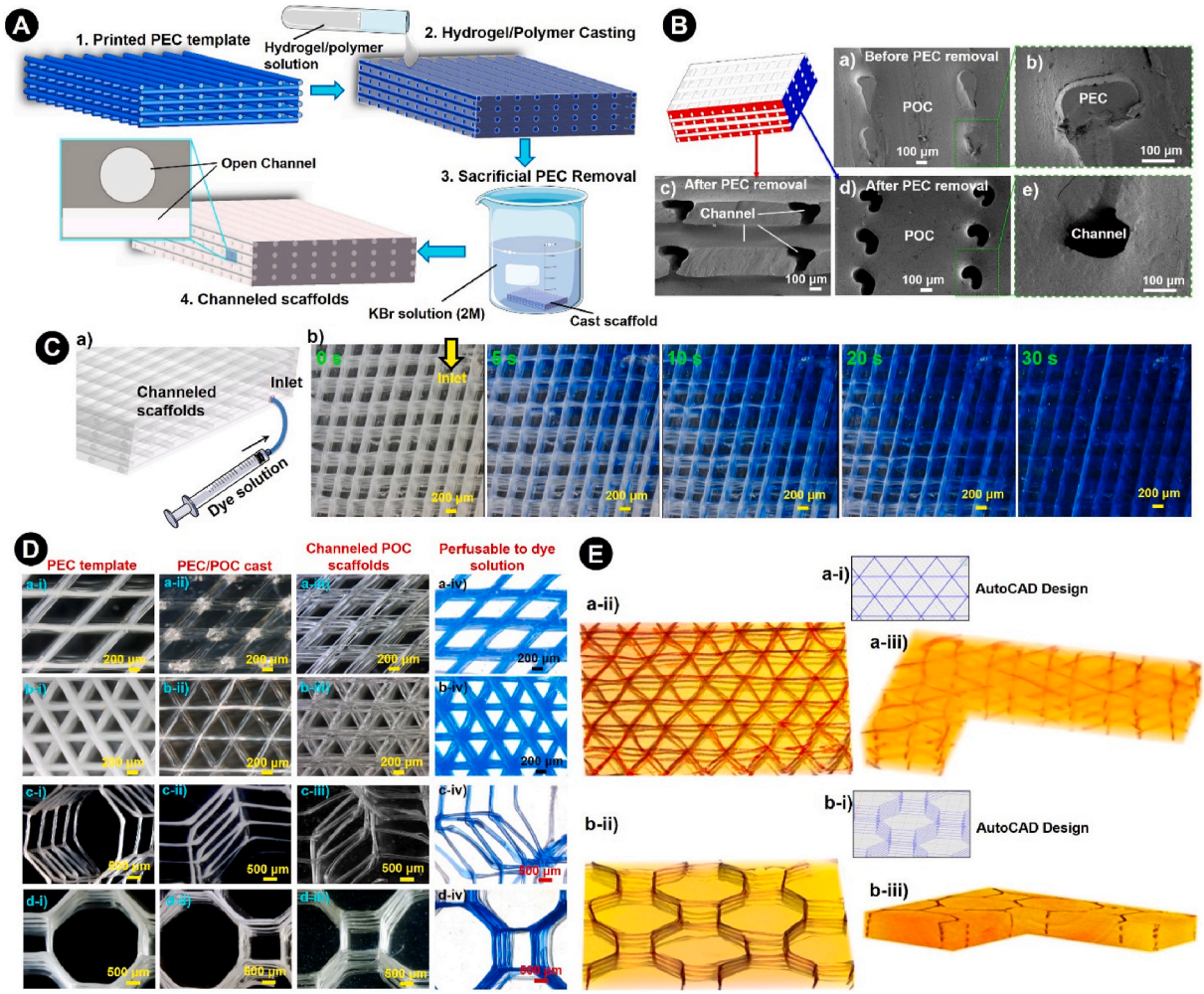

Fig. 5. Formation of the channeled POC scaffolds with patent and versatile luminal networks. A) Schematic illustration of the PEC template-assisted formation of interconnected channel networks within the POC cast upon ready removal of the PEC template with concentrated KBr aqueous solution. B) SEM micrographs of the cross-sections of POC cast with microchannels before and after PEC template removal. Scale bar: 100 μm. C) Characterization of the permeability of interconnected microchannels within the POC cast, in which the experimental setup was illustrated in C-a) and time-lapse infiltration of the dyed solution (blue) through the channels was shown in C-b). Scale bar: 200 μm. D) Microscopic images (a-iii to d-iii) and permeabilities (a-iv to d-iv) of channeled POC scaffolds with various channel organizations, which were generated by removing the PEC templates (a-i to d-i) from the PEC/POC cast (a-ii to d-ii). Scale bar: a-b) 200 μm; c-d) 500 μm. E) Confirmation of the formation of desirable open microchannels (red) within POC (yellow) similar to the original design (a-i to b-i) based on the top view (a-ii to b-ii) and side view (a-iii to b-iii) via Micro-CT scanning.

guidelines for the ethical treatment of animals. Twelve Sprague-Dawley rats (SD, male, 180 g) bred at the local animal care facility were used for the subcutaneous implantation. The rats were anesthetized with 2% pentobarbital via abdominal injection. For subcutaneous implantation, two subcutaneous pouches (1 cm long) were created by dissecting the posterior dorsum skin of rats. Cubic SF scaffolds (8 mm × 8 mm × 2 mm) with channels (Scaffold A: CD 200 μm, ICD 800 μm; Scaffold B: CD 200 μm, ICD 600 μm; Scaffold C: CD 400 μm, ICD 800 μm) or without channels were placed into each pouch, and the skin incision was sutured with 3/0 Mersilk (Ethicon, UK). The rats were sacrificed at the designated time points (14 and 28 days post-implantation), and the implanted scaffolds (n = 3 per group) were explanted for further analyses. The harvested explants were longitudinally cut into two parts and examined under a stereomicroscope. Then both were fixed with 2.5% glutaraldehyde and 4% PFA for histochemical staining and immunofluorescence staining.

2.12. Immunohistochemical and immunofluorescence staining

The explanted specimens embedded in OCT were cut into 6-μm sections. The thin sections were performed for H&E staining. Immunofluorescence staining was also performed to investigate the vascularization and the inflammatory reaction. Sections were blocked with 5% bovine serum albumin (BSA) for 1 h at room temperature, and immunolabeled with primary antibodies: rabbit anti-von Willebrand factor (vWF) (ab6994, 1:100, Abcam), rabbit anti-CD206 (1:1000, Abcam) and rabbit anti-iNOS (ab15323, 1:500, Abcam). Alexa Fluor 488 goat anti-rabbit IgG (1:200, Invitrogen) and Alexa Fluor 594 goat anti-mouse IgG (1:200, Invitrogen) were used as the secondary antibodies, respectively. Nuclear staining was performed by incubating the sections with a Vecta shield mounting medium containing 4,6-diamidino-2-phenylindole (DAPI, H-1200, Vector Labs). Stained sections were examined under the Zeiss Axio Imager Z1 epi-fluorescence microscope (Carl Zeiss, Inc., Oberkochen, Germany) and quantified using Image-J software.

2.13. Statistical analysis

All the in vitro quantitative data were obtained from at least triplicates or measurements, and experiments were separately repeated three times. Data were expressed as the mean ± standard deviation (SD). All

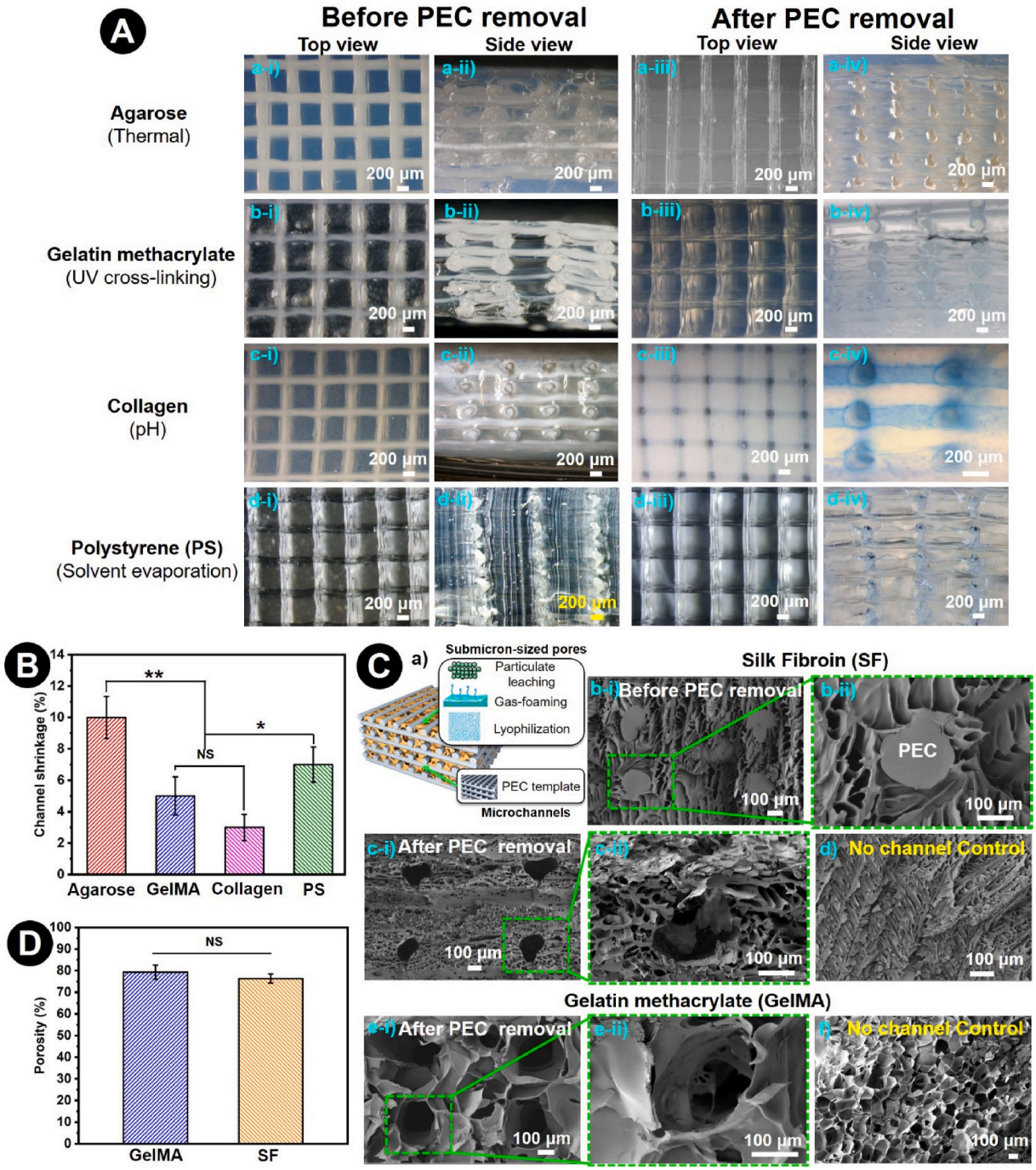

Fig. 6. Formation of channeled scaffolds from versatile castable biomaterials. A) Microscopic images of the channeled scaffolds prepared from agarose (Aa), gelatin methacrylate (GelMA) (Ab), collagen (Ac) and PS (Ad) before (a-i&ii to d-i&ii) and after (a-iii&iv to d-iii&iv) the removal of sacrificial PEC templates. B) Quantification of the channel shrinkage within different materials after PEC removal. ($n \geq 5$, $^{*}p < 0.05$, $^{**}p < 0.001$, NS: not significant). C) Development of channel networks in combination with other porogenic methodology (e.g., particulate leaching, lyophilization, gas-foaming) (Ca) to form channeled scaffolds with multiscale porous structures as demonstrated with SF (Cb-d) and GelMA (Ce-f) after lyophilization. SEM micrographs of PEC template embedded in SF cast materials (Cb-i and ii) and the formation of microchannels among lyophilized pores after PEC template removal (*Cc*-i and ii) as compared to SF lyophilized scaffolds without channels (Cd). SEM micrographs of the channeled GelMA scaffolds with additional lyophilized pores (Ce-i and ii), different from those without channels (Cf). Scale bar: 100 μm. D) Comparable porosity between GelMA and SF microchanneled scaffolds with lyophilized pores as determined by Micro-CT scanning. ($n \geq 5$, NS: not significant).

the collected data were analyzed using unpaired t-tests or one-way analyses of variance (ANOVA) with Scheffe's post hoc test of the statistical software SPSS, Version 10.0 (SPSS, Chicago, IL, USA), and $p < 0.05$ was considered statistically significant.

3. Results and discussion

3.1. Preparation and characterization of printable PEC inks

A critical step toward the sacrificial template-assisted formation of channel structures within the cast is to identify the appropriate

Table 2
Parameters of scaffolds.

Group	Porosity (%)	Channel Diameter (μm)	Inter-Channel Distance (μm)
Control	22.5 ± 5.4	no	no
Scaffold A	65.7 ± 2.8	200	800
Scaffold B	76.4 ± 2.1	200	600
Scaffold C	82.6 ± 3.8	400	800

formulation of PEC materials used for EB3DP to generate the sacrificial templates with arbitrary patterns. As shown in Fig. 2A, mixing PDADMAC and PSS at a concentration of 2.50 M with respect to their monomer units at a volume ratio of 1:1 led to rapid complexation (<1 min) via the intrinsic electrostatic interactions, and the maximum PEC complexation was achieved with an equal molar ratio (Fig. S1, Supplementary), consistent with the previously reported combination molar ratio of 1.032 [37]. No involvement of chemical cross-linking agents during complexation has been considered beneficial, which not only eases the manufacturing process but also minimizes any possible toxicity and undesirable effects. Upon centrifugation at 10,000 rpm for 15 min, the PDADMAC/PSS PEC precipitate was readily separated from the reaction. As recognized, coupled ion pairs (i.e., Pol^+ Pol^-) of the polyelectrolyte chains in PEC could be gradually broken with the addition of salt, in which the salt counterions (i.e., $M_{aq}{}^+$ and $A_{aq}{}^-$) progressively paired with the PEC segments to decouple the established physical cross-links. The process can be illustrated with Equation (1) [38].

$$Pol^+ Pol^- + M_{aq}{}^+ + A_{aq}{}^- \rightleftharpoons Pol^+ A^- + M^+ Pol^- \quad (1)$$

Heoretically, many types of salts can be used to partially or completely dissociate the PEC and render tunable viscosity. The dissociation speed significantly relies on the strength of PEC pairs, ionic diffusion coefficient, and salt dissociation. With a diffusion coefficient of about 10^{-6} cm^2 s^{-1}, potassium bromide (KBr) was particularly chosen in this study for its demonstrated capability of reaching the doping equilibrium faster than sodium chloride [39,40]. As shown in Fig. 2B, with the increase of KBr concentration, the PDADMAC/PSS complex was gradually compensated with counterions (i.e., K^+ and Br^-) from the 'extrinsic sites' of PEC [41]. At a lower KBr concentration (≤1.50 M KBr), the PEC was plasticized while remaining physically intact. When the KBr concentration increased to 1.75 M, the PEC turned into a viscous liquid (known as 'coacervate') with the viscosity appropriate for extrusion printing without blocking the printing nozzle as a result of shear-induced pressure drop (Fig. 2C). With a further increase of KBr concentration (≥2.00 M KBr), the pre-coupled Pol^+ Pol^- pairs of PDADMAC/PSS in PEC were completely dissociated by the KBr counterions to form a homogenous solution. Recognizing the essential contribution of coacervate viscosity to its printability and printing resolution motivated our further efforts to possibly tune the viscosity by soaking the same amount (1.2 g) of molded dry PEC in different volumes (i.e., 1, 4, and 8 mL) of 1.75 M KBr solutions. In contrast to 4 mL and 8 mL (Fig. S2, Supplementary), which yielded the formation of semi-transparent coacervate on the bottom, 1 mL was not enough to submerge the PEC and only led to its partial plasticization. To our surprise, increased KBr volume did not render more coacervate or reduce the viscosity, and instead, a comparable volume of coacervate with similar viscosity was obtained. Measurement of the supernatant conductivity also confirmed no changes in KBr concentration. All these observations suggest a close regulation of PEC coacervate viscosity primarily by the KBr concentration. Indeed, in the range of 1.65–1.85 M KBr, the viscosity decreased with the increase of KBr concentration (2767 Pa s vs. 330 Pa s at 16 s^{-1}, Fig. S3, Supplementary). A clear boundary could be oftentimes seen between the PEC coacervate (at the bottom) and the rest solution (Fig. S2A, Supplementary). As such, the viscous PEC coacervate could be easily collected by discarding the supernatant and then used for printing. In addition, the shear applied to the coacervates during printing would substantially decrease the viscosity, i.e., the typical shear-thinning phenomena (Fig. 2C), for easy extrusion. In order to better identify the optimal viscosity range for PEC printing linked to various shearing conditions in the extrusion manner, the shear rate range was therefore calculated using Equation (2).

$$\dot{\gamma} = \frac{4Q}{\pi r^3} \quad (2)$$

where Q is the volumetric flow rate; r is the inner radius of printing nozzle, which was 26 G needle with 130 μm inner radius; $\dot{\gamma}$ is the shear rate.

A shear rate from 16 s^{-1} to 193 s^{-1} was obtained based on the volumetric flow rate (from 0.1 mL h^{-1} to 1.2 mL h^{-1}), which was the working setup for our customized 3D printer. We established a quantitative phase diagram (Fig. 2C) to rationally select the printable PEC/KBr coacervate viscosity range with the preset shear rate range. In the case of PEC/KBr (1.75 M) coacervate, a viscosity range between 1089 Pa s and 604 Pa s of the resulting shear-thinning fluid enables continuous and uniform extrusion of PEC filament. As noted, extruding the PEC coacervate into deionized water led to instantaneous solidification into filaments (Movie S1, Supplementary), which most likely resulted from the rapid diffusion of KBr out of the coacervate. More specifically, an osmotic gradient developed between the extruded coacervate and surrounding water drives the diffusion of KBr ions out of the PEC, leading to the plasticization and stretching of PEC filaments. Previous studies have suggested diffusion of counterions (i.e., K^+ and Br^-) is at least two orders of magnitude faster than the diffusion of polyelectrolytes themselves [41,42]. However, their diffusion was also closely regulated by the osmotic gradient and the distribution of counterions across the extruded PEC coacervate. For example, PEC doped with 1.85 M KBr exhibited higher osmotic pressure than that with 1.65 M KBr, which accelerated the diffusion of the counterions located in the superficial region of extruded PEC coacervate and led to rapid re-complexation of PDADMAC/PSS for solidification [40–43]. Formation of the dense PEC outer shell would limit further effective diffusion of those counterions in the interior region and water inside out. Such distinct diffusion profiles unavoidably led to the development of two phases within the PEC filaments, i.e., a porous core and a dense shell (Fig. S4A, Supplementary) [44]. As anticipated, the 'shell thickness' of PEC filaments would decrease with the increase of KBr concentration (Fig. S4B, Supplementary). In contrast, the PEC coacervate doped with 1.65 M KBr would have sufficient time for the counterions to diffuse across the entire filament thickness and form a uniform solid filament. As such, the filaments of 1.65 M KBr coacervates would be much more rigid than those of 1.85 M ones (Fig. S4C, Supplementary) with the soft and porous core. Due to the presence of a large watery core in PEC filaments of 1.85 M coacervates, it is not hard to understand why a relatively larger filament diameter was seen after printing, and a higher shrinkage rate was measured after drying compared to those of 1.65 M and 1.75 M coacervates (Fig. S4D, Supplementary). These observations also suggest that it is possible to tune the PEC filament diameter and properties to a certain degree. Considering the acceptable pressure resistance during extrusion printing, relatively small filament shrinkage after drying, and good mechanical rigidity, 1.75 M KBr PDADMAC/PSS coacervate was chosen for further EB3DP. Next, to determine the capability of modulating filament diameter with 1.75 M PEC coacervate and its related structural fidelity, cross-sections of filaments with different diameters (75–460 μm) from the same 1.75 M KBr-PEC coacervate were examined. As shown in Fig. S5A (Supplementary), the filaments with the diameter larger than 175 μm exhibited the core-shell structure and then disappeared when the filament diameter was reduced to 115 μm. A similar dense shell thickness from 50 ± 2 μm to 52 ± 4 μm was obtained when the filament diameter varied from 175 μm to 460 μm, simply because of a constant counterion diffusion coefficient of the 1.75 M KBr-doped PEC coacervate. Clearly, those filaments with a diameter of two times of the

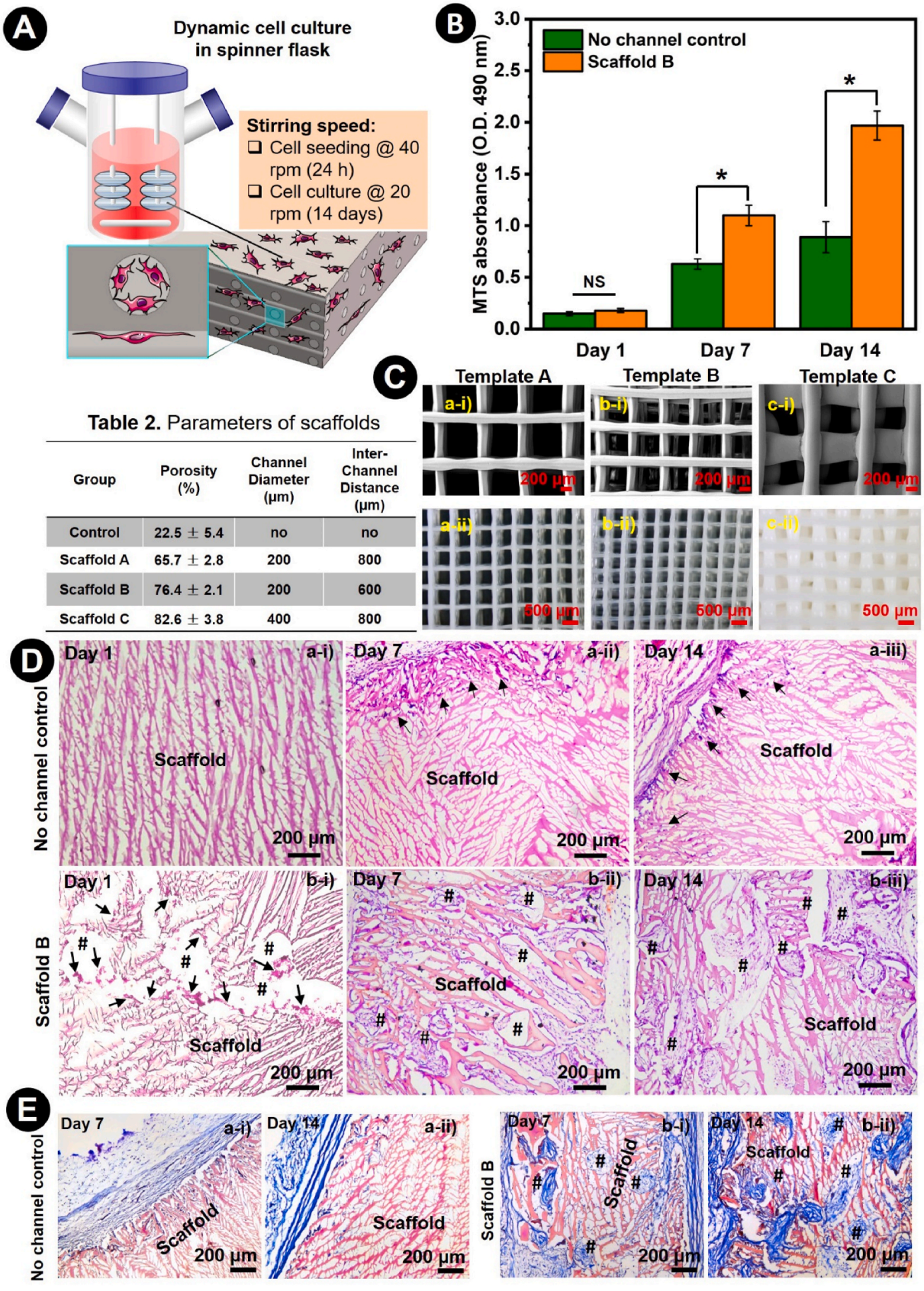

Table 2. Parameters of scaffolds

Group	Porosity (%)	Channel Diameter (μm)	Inter-Channel Distance (μm)
Control	22.5 ± 5.4	no	no
Scaffold A	65.7 ± 2.8	200	800
Scaffold B	76.4 ± 2.1	200	600
Scaffold C	82.6 ± 3.8	400	800

(caption on next page)

Fig. 7. In vitro cultivation of mouse fibroblasts (STO cells) within the channeled and lyophilized SF scaffolds to evaluate their supportiveness of tissue formation. A) Schematic illustration of the cell seeding and continuous cultivation conditions within a spinner flask. B) Quantitative analysis of the attachment and proliferation of STO cells within the Scaffold B and non-channeled control after culture for 1, 7, and 14 days. Cell proliferation was indirectly measured by MTS assay. ($n \geq 5$, $^*p < 0.05$, NS: not significant). C) Morphology of the respective PEC template (A, B, C) used for the creation of different channeled scaffolds (A, B, C). ai-ci) SEM micrographs of PEC templates. Scale bar: 200 μm aii-cii) Stereo microscopic images of PEC templates. Scale bar: 500 μm. The key attributes of different scaffolds are summarized in Table 2. D) Representative microscopic images of H&E stained cross-sections of the cultured constructs to show cell distribution and tissue formation within non-channeled control (Da) and the Scaffold B (Db) after culture for 1, 7, and 14 days. Scale bar: 200 μm #: transverse section of channels. Black arrow: cells and newly formed tissue. D) Representative microscopic images of the Masson's trichrome stained cross-sections of the cultured constructs to better show the newly synthesized collagen (blue) within non-channeled control (Ea) Scaffold B (Eb) and after culture for 7 and 14 days. Scale bar: 200 μm #: transverse section of channels.

shell thickness or less would see a uniform solid structure. Although even smaller filament diameter (e.g., 75 μm) could be achieved, filament deformation and flattening (Fig. S5A, Supplementary) did occur due to the stretch of PEC coacervate while the nozzle tip was moving through the supporting matrix.

Supplementary data related to this article can be found at https://doi.org/10.1016/j.bioactmat.2022.01.030.

In view of the unique reversible solidification/dissolution of PEC (PDADMAC/PSS) via the addition of water or concentrated KBr, it not only provides the opportunity to modulate PEC coacervate with suitable viscosity and solidification speed as the printing ink for fabricating 3D stable structure, but also offers a convenient and 'green' means to remove and recycle PEC as the sacrificial template for creating arbitrary channels within various substrates. As illustrated in Fig. 2D, PEC scaffolds could quickly dissolve in 2.00 M KBr solution and reprecipitate upon reducing the KBr concentration. After centrifugation and rinse with water, the precipitated PEC could be collected and redissolved in 1.75 M KBr to form the printable coacervate, offering an eco-friendly and cost-effective platform for both laboratorial and industrial manufacturing.

3.2. Fabrication of 3D PEC templates via EB3DP in pluronic F127

To enable EB3DP of PEC microfiber with arbitrary spatial organizations, a triblock copolymer, Pluronic F127, i.e., polyethylene oxide (PEO)-polypropylene oxide (PPO)-polyethylene oxide (PEO), was particularly used as the supporting matrix (Fig. 3A) to benefit from its unique thermoreversible gelation behavior [30]. Above the critical micelle temperature (CMT), the amphiphilic PEO-PPO-PEO triblock structure of aqueous Pluronic F127 solution could self-aggregate to form spherical micelles with the hydrophobic PPO core surrounded by hydrophilic PEO corona. The concentration and temperature-dependent micellization of Pluronic F127 has been extensively investigated [28,45]. Here, 25% (w/v) Pluronic F127 aqueous solution was particularly chosen for EB3DP for its gelation at room temperature (CMT is ~22 °C) while exhibiting the 'shear-thinning capability, i.e., dramatic decrease of the shear stress following the increased shear rate of the moving printing nozzle. In this regard, we tested the changes of the storage modulus in relation to the shear stress. As shown in Fig. 3C, the storage modulus of 25% (w/v) Pluronic F127 (approx. 30 kPa) decreased with the increase of shear stress, indicating its capability of locally liquifying via shear-induced thinning for the printing nozzle to move freely through and then gelating with the recovery of the storage modulus from the shear reduction to zero. Other concentrations were also evaluated, e.g., 20% (w/v) Pluronic F127 remained as a liquid-like solution all the time, and the low storage modulus determined its unsuitability as a supporting matrix. The noted shear-thinning property, on the other hand, also endowed 25% (w/v) Pluronic F127 with the self-healing ability to immediately fill up the void caused by the fast movement of the printing nozzle and prevent potential deformation of the printed constructs from the moving nozzle (Fig. 3B). The presence of excessive water in 25% (w/v) Pluronic F127 also enabled rapid solidification of the printed PEC coacervate into filaments. In addition, the thermo-responsive phase transition of Pluronic F127 would allow for convenient extraction of the printed PEC constructs for later casting (Fig. S6, Supplementary). Below CMT, Pluronic F127 rapidly converted into an aqueous solution to free the printed constructs and be readily removed after rinsing.

With the established conditions (i.e., 25% (w/v) Pluronic F127 as supporting matrix and 1.75 M KBr-doped PEC coacervate as printable ink), we first investigated the controllability and other associated boundary conditions for EB3DP. Fig. 3B schematically illustrated the setup of EB3DP, in which the PEC ink was extruded at a pumping rate V_p out of a moving nozzle (26G) with an inner diameter D_n and a moving speed V_a. During the printing, the void caused by the moving nozzle in the supporting matrix could be rapidly filled with the stream of micelles from the surrounding via shear-thinning (*a.k.a*, self-healing) to protect the printed constructs (Fig. 3B inset). Besides, a die swell, i.e., the printed filament diameter D' was larger than D_n, was expected resulting from a combinatory effect of its elasticity and the associated shear-thinning of the extruded PEC coacervate. This die-swell phenomenon would undoubtedly restrict the filament diameter D' from a smaller size and consequently constrain the printing resolution. Fortunately, such a limitation could be partially overcome by plasticization and stretching of the PEC coacervate within the 25% (w/v) Pluronic F127 during EB3DP. As illustrated in Fig. 3E, a solidified PEC layer would be instantaneously formed to wrap around the extruded PEC ink droplet following the die-swell phenomenon, owing to uneven ionic exchange of counterions between PEC coacervate and 25% (w/v) Pluronic F127. The intrinsic difference in elastic modulus between PEC coacervate ink and Pluronic F127 supporting matrix allowed stretching the printed PEC coacervate into filament with a uniform diameter D. The process also facilitated the ion diffusion to prevent from beading or dragging the printed structure around (Fig. 3D). Eventually, a steady state of plasticization/stretching in conjunction with a delicate balance of water content, recoupled PEC pairs, and surrounding counterions (Fig. 3E) would allow fabricating a printed PEC structure with high fidelity and good mechanical stability. With the selected supporting matrix and PEC coacervate, the printability of PEC filaments in EB3DP was closely related to the ratio between extrusion pumping rate (V_p) and nozzle moving speed (V_a). By respectively modulating V_a and V_p, a color-coded map was therefore generated to indicate the suitable V_a and V_p for the possible formation of the stable filament (Fig. 3F) under our customized printing conditions, which well corresponded to the circumstances as illustrated in Fig. 3D. Furthermore, a correlation was established between filament diameter and V_p/V_a ratio (Fig. 3G). With the V_p/V_a ratio larger than 0.67 μL mm^{-1}, excessive PEC coacervate accumulated on the tip of the printing nozzle due to a relatively slow printing speed, causing the destruction of the printed structure. On the other hand, when the V_p/V_a ratio was lower than 0.008 μL mm^{-1}, the fast traveling nozzle would drag the limited PEC coacervate through the supporting matrix, leading to flat and thin filament or even bead formation.

With the V_p/V_a ratio ranging from 0.008 to 0.67 μL mm^{-1}, the filament diameter was tunable and increased over the V_p/V_a ratio, which was somewhat independent of the nozzle size. The high printing fidelity allowed to control the inter-filament distance (Fig. 4Ab) as small as 20 μm while modulating the filament diameter from 120 to 500 μm (26G printing nozzle (φ_{inner} = 260 μm) was used) (Fig. 4Aa). The proven possibility of reaching a much finer filament diameter (as small as 75 μm) (Fig. S5, Supplementary), beyond the limits of conventional extrusion 3D printing (e.g., 100 μm), would significantly enhance the printing resolution [46]. The printed filaments had a rather smooth surface (Fig. 4Ba-b). Different from the uniform solid transverse section

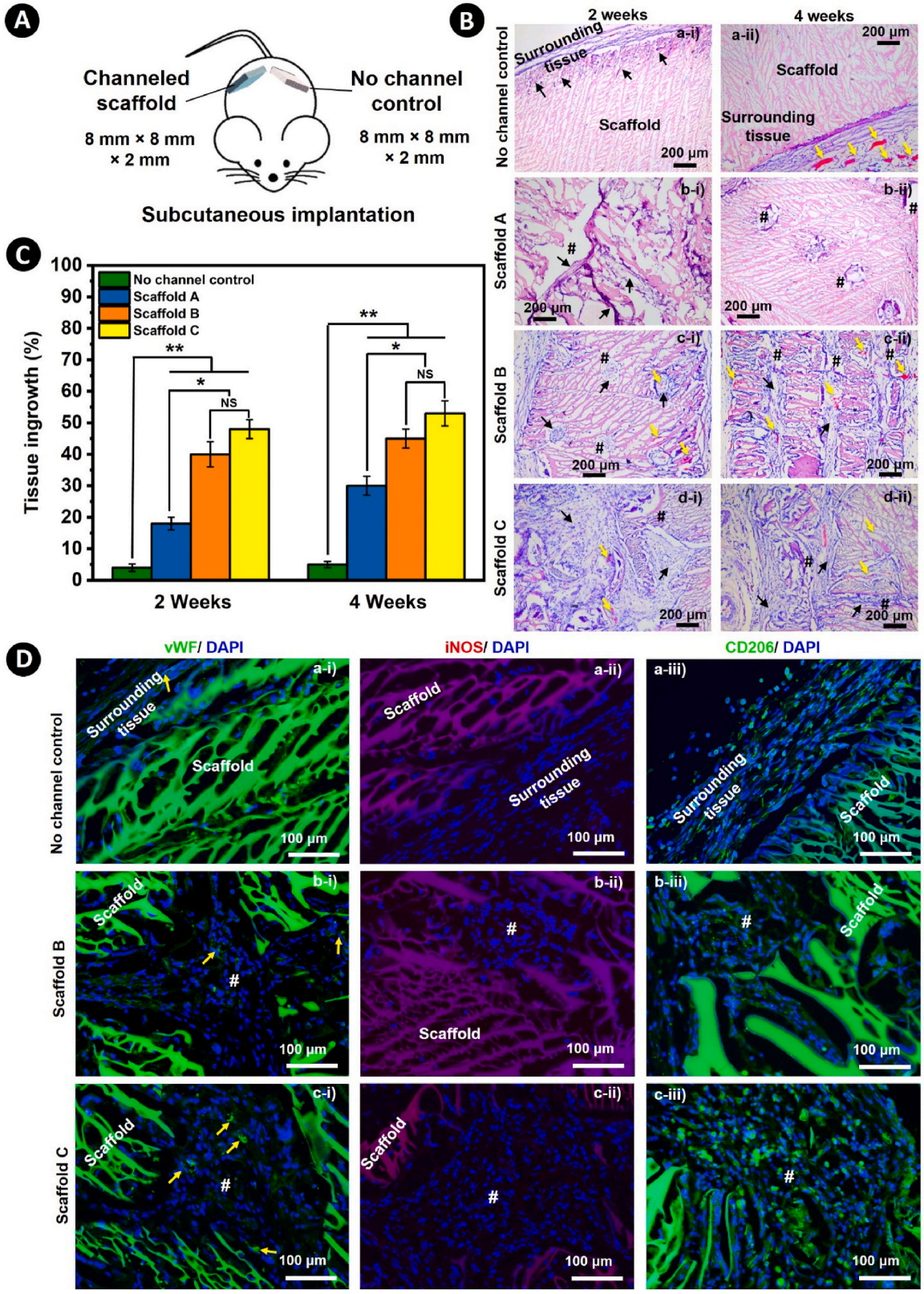

Fig. 8. In vivo implantation of various channeled and lyophilized SF scaffolds to evaluate the effect of microchannels on tissue ingrowth. A) Schematic illustration of the experimental setup, in which either channeled scaffolds (Scaffold A, B, and C) or non-channeled scaffolds (control) were implanted subcutaneously into the rats. B) Representative microscopic images of the H&E stained cross-sections of explants after subcutaneous implantation for 2 (Ba-i to Bd-i) and 4 (Ba-ii to Bd-ii) weeks. Scale bar: 200 μm #: transverse section of channels. Black arrow: newly formed tissue. Yellow arrow: newly formed capillaries. C) Semi-quantification of the tissue ingrowth within different scaffolds after subcutaneous implantation for 2 and 4 weeks. ($n \geq 5$, $^{*}p < 0.05$, $^{**}p < 0.001$, NS: not significant). D) Representative fluorescence images of cross-sections of the explants for new vessel formation (Da-i to Dc-i) upon immunofluorescently staining for vWF (green) and DAPI (blue), pro-inflammatory macrophages (Da-ii to Dc-ii) upon immunofluorescently staining for iNOS (red) and DAPI (blue) and anti-inflammatory macrophages (Da-iii to Dc-iii) upon immunofluorescently staining for CD206 (green) and DAPI (blue). Scale bar: 100 μm #: transverse section of channels. Yellow arrow: newly formed capillaries.

of small diameter filaments (i.e., 75–120 μm), increased diameter (>120 μm) of filaments did show the core-shell structure (Fig. 4Bc-e, S5, Supplementary) with better handleability. For convenience, we chose a diameter of 200 μm for the subsequent studies. To demonstrate the printing versatility and accuracy, we explored printing PEC filaments with various overlay angles (15°, 30°, 45°, 60°, 75°, and 90°) (Fig. 4Ca-f), complex patterns (triangle, wave, and honeycomb) (Fig. 4Cg-i) and multiple layers of stacking (Fig. 4Cj-l). In particular, the multilayer PEC honeycomb patterns were printed in a continuous and layer-by-layer fashion with a large dimension (2 cm × 2 cm × 0.3 cm). Clear boundaries for each layer (Fig. 4Cl) demonstrated the established EB3DP for ready scaleup to produce large and complex structures. Clearly, all the printed PEC constructs showed a well-controlled structure with high fidelity. The mechanical properties of printed 3D PEC constructs might vary over different configurations and water contents. Compared to hydrogel- and sugar melt-based structures, the printed 3D PEC constructs exhibited moderate mechanical strength with good flexibility [21,24]. Cyclic compression test was performed to the dry 10-layer PEC grids (Fig. 4Da) with 90° overlay angle loaded either from the top or from the side (Fig. 4Db-c, Movie S2, and Movie S3, Supplementary), demonstrating the capability of recovering from deformation without delamination or structural collapse. Besides the dry state, wet 6-layer PEC honeycomb constructs were also evaluated for their elasticity and structural stability by manually folding with forceps (Fig. 4E). As a matter of fact, the tested properties are essential for the use of printed PEC constructs as sacrificial templates in different casting platforms.

Supplementary data related to this article can be found at https://doi.org/10.1016/j.bioactmat.2022.01.030.

3.3. Formation of microchannel networks within poly(1, 8-octanediol-co-citrate) (POC) casts

The formation of interconnected channels within the cast is closely regulated by the printing resolution, structural stability, and ready removal of sacrificial templates, especially for the hierarchical multichannel network (Fig. 5A). Thus, we sought to determine the suitability of printed PEC structures as sacrificial templates for generating perfusable open microchannels within poly(1, 8-octanediol-co-citrate) (POC) [47], a recently developed biodegradable and biocompatible polyester elastomer with the difficulty of manufacturing its porous scaffolds [48,49]. Briefly, POC right after synthesis from 1,8-octanediol and citrate (at a molar ratio of 1:1) at 140–165 °C under nitrogen atmosphere was directly cast into a mold with 8-layer 90° overlayed PEC grids and then cooled down to solidify in a 100 °C vacuum oven. To better visualize the PEC template within the POC cast, the cross-section was examined under SEM. The PEC filaments could be easily identified, and a circular-to-oval deformation was seen (Fig. 5Ba-b), which was most likely due to the high temperature and vacuum-induced dehydration of PEC filaments. The time required for PEC removal is dependent on the PEC pairs and the counterions. With PDADMAC/PSS and 2.00 M KBr in our experimental setup, the dissolution of the PEC template out of the POC cast happened in the order of minutes (Fig. 2D). After incubation within 2.00 M KBr aqueous solutions for 15 min, complete removal of PEC templates from the POC cast was confirmed with SEM examination of the cross-section, and open microchannels were developed (Fig. 5Bc-e). In a separate experiment, we also confirmed that the remnant KBr in POC cast could be efficiently removed after rinsing with deionized water five times, as determined by conductivity measurement of the supernatant (Fig. S7, Supplementary). Additional shrinkage of the open channels was observed, approx. 6.1 ± 0.2% of the original filament transverse area, which might result from the elastic contraction of POC itself (Fig. S8, Supplementary). As confirmed, these microchannels were well connected at the junction of overlayed PEC filaments (Fig. 5Bc). To better evaluate the interconnectivity and efficiency of microchanneled architectures for mass transport, a Coomassie Brilliant Blue solution (0.025%, w/v) was injected (at a speed of 2 mL h^{-1}) through the opening at the bottom of the channeled POC cast (Fig. 5Ca). Time-resolved infiltration of the dye throughout the entire channels readily took place in a layer-by-layer manner (Fig. 5Cb and Movie S4, Supplementary). Similarly, the printed PEC templates with other configurations were also tested for their capability of generating versatile open channeled structures within the POC cast (Fig. 5D). Once again, after the removal of PEC templates, the microchannels were well connected to each other and perfusable to the dye solution (Fig. 5Da-iv-d-iv and Movie S5-S6, Supplementary). Micro-CT analysis was also performed on the channeled POC scaffolds to better visualize the spatial organization of the lumens. As shown in Fig. 5E and Movie S7-S9 (Supplementary), these microchannels formed by PEC templates (labeled in red) displayed a 3D hierarchical structure, closely following the AutoCAD designs. These results evidently indicate that a 3D complex microchannel network could be efficiently and reliably formed within the POC cast with the aid of sacrificial PEC templates and may allow for free mass/oxygen transport via the physiologically relevant perfusion.

Supplementary data related to this article can be found at https://doi.org/10.1016/j.bioactmat.2022.01.030.

3.4. PEC-templated microchannel formation within diverse castable materials

To further determine the flexibility and generality of this PEC-templating approach, we explored to create perfusable microchannels in other commonly used natural (e.g., agarose and collagen) or synthetic (e.g., GelMA and polystyrene) materials (Fig. 6A). More importantly, these casting materials, relying on different means to solidify (i.e., pH- and thermo-responsive gelation, UV-induced cross-linking, and organic solvent evaporation), did not cause noticeable destruction to the PEC templates (i.e., 5-layer 90° overlayed grids) (Fig. 6Aa-d-i&ii). Incubation of these cast blocks with 2.00 M KBr solution to dissolve away the PEC templates did not impact the structural integrity of the channeled scaffolds. Similar to POC, thermo-induced microchannel deformation was also observed with agarose (Fig. 6a–iv). In contrast, circular channels were obtained with the rest of the materials (Fig. 6Aa-d-iii and -iv). Interestingly, different shrinkage rates of microchannels from the PEC filaments (200 μm in diameter) were observed depending on the cast materials. Analysis of the microscopic images with ImageJ revealed the highest shrinkage (10.4%) with agarose followed by polystyrene (PS, 7.2%), GelMA (5.3%), and collagen (3.7%) (Fig. 6B). The noted variation in microchannel sizes most likely results from water loss of the printed PEC templates during the solidification processes of cast materials. Clearly, organic solvent evaporation (chloroform for PS) and high-temperature processing (120 °C for agarose) would inevitably reduce the water contents of the PEC template in comparison to the hydrogels (GelMA and collagen). Despite the shrinkage, PEC templates consistently supported the development of open and interconnected microchannels in these matrices. To our knowledge, no other reported sacrificial templates demonstrated to be compatible with such a broad range of castable materials. Moreover, the PEC-templated channel formation could also be readily combined with other porogen-based methods (e.g., lyophilization, gas-foaming, and particulate leaching) to fabricate scaffolds with interconnected hierarchical channels among the pores (Fig. 6Ca). For instance, removal of the PEC templates from a 40% (w/v) silk fibroin (SF) sponge after lyophilization and glutaraldehyde cross-linking led to the formation of microchannels among micron- and submicron-sized pores (2–20 μm) of SF matrix (Fig. 6Cb-c). Similarly, PEC-templated microchannels could be formed among micro-sized pores (40–80 μm) within cross-linked 10% GelMA after lyophilization (Fig. 6Ce). MicroCT analysis of the resultant scaffolds revealed comparable porosity between SF scaffolds (76 ± 2%) and GelMA scaffolds (79 ± 3%) despite distinct lyophilized pores around the microchannels (Fig. 6D).

3.5. In vitro tissue formation within channeled scaffolds

The introduction of microchannels into lyophilized sponges is anticipated to not only facilitate mass exchange throughout the sponge, but also support cell infiltration and tissue formation. Here, three types of channeled SF scaffolds (designated as Scaffold A, B, and C) with various channel diameters (CD) (200 or 400 μm) and inter-channel distances (ICD) (600 or 800 μm) and non-channeled SF scaffolds (controls) (Table 2) were selected to attest the microchannel-encouraged tissue formation. The PEC templates used to generate such channeled scaffolds were shown in Fig. 7C. For in vitro cell cultivation, lyophilized SF cubes (8 mm × 8 mm × 2 mm) without (controls) or with microchannels (Scaffold B, CD = 200 μm, ICD = 600 μm) were dynamically seeded with mouse fibroblasts (STO cells, 1×10^5 cells/scaffold) and then cultured under a continuous stirring in a spinner flask (Fig. 7A), which demonstrated its capability of achieving even cell distribution among scaffolds and its supportiveness for continuous cell proliferation and ECM deposition [50]. A comparable number of cells determined by the metabolic activities via MTS assay were initially seeded onto Scaffold B or non-channeled SF scaffolds. However, significantly elevated cell proliferation was observed only with channeled SF scaffolds at day 7 and 14 (Fig. 7B). H&E staining of the cross-sections of cultured constructs also revealed more cells and new tissues located in the interior pores, primarily through the microchannels (Fig. 7D). To better visualize new ECM deposition, cross-sections were also performed with Masson's trichrome staining for collagen. As shown in Fig. 7E, deposition of newly synthesized collagen (blue) only occurred to the peripheral regions of non-channeled SF scaffolds. Although the pores within non-channeled SF sponges favor mass exchange, the sizes might be too small for the cells to infiltrate. In contrast, a significant amount of collagen was seen throughout the microchannels of Scaffold B, confirming the efficiency and benefits of such microchannels in facilitating mass exchange and supporting new tissue formation.

3.6. In vivo tissue formation and vascularization within channeled scaffolds

To evaluate the efficacy of channeled scaffolds for tissue ingrowth and explore the correlation of various configurations (i.e., CD and ICD) with cellularization, vascularization, and immunoregulation, channeled SF scaffolds (Scaffold A, B, and C) and non-channeled SF scaffolds (controls) were selected for subcutaneous implantation to the dorsal area of Sprague-Dawley rats (Fig. 8A). Compared to non-channeled ones, all three channeled scaffolds exhibited significantly increased porosity determined by MicroCT analysis. The porosity was further improved by increasing the channel diameter and density (Table 2). Histological analysis (H&E staining) of the explants after 2 and 4 weeks' implantation revealed tissue ingrowth of the channeled scaffolds primarily through the channels evidently seen with scaffold A (Fig. 8Bb), which had a small CD (200 μm) and large ICD (800 μm). An increase of CD (Scaffold C) or decrease of ICD (Scaffold B) was able to promote tissue ingrowth (Fig. 8Bc and d) significantly. Minimal tissue ingrowth occurred to the non-channeled scaffolds, only in the superficial region or just around the scaffolds (Fig. 8Ba). Along with tissue ingrowth, efficient angiogenesis is also essential to vitalize newly formed tissues [51,52]. As reported, vascularization of scaffolds is closely regulated by the size and interconnectivity of pores, and 200–400 μm is the appropriate pore size range for vascularization, which is consistent with the microchannel size (200–400 μm) [53–55]. In contrast to limited microvessels within the non-channeled scaffolds or Scaffold A, an elevated number of microvessels were identified in Scaffold B and C (yellow arrows). To better visualize the vasculature, immunofluorescence staining for von Willebrand factor (VWF) was also performed. As indicated by the yellow arrows in Fig. 8, more capillaries were formed through the microchannels of scaffolds B and C. Clearly, cell infiltration and vascularization both correlated well with the interconnected microchannels and increased porosity. Image analysis revealed 18% (Scaffold A), 40% (Scaffold B), and 48% (Scaffold C) tissue ingrowth of the channeled scaffolds respectively after 2 weeks' implantation, significantly higher than that (4%) of non-channeled scaffolds (Fig. 8C). Upon implantation for another 2 weeks, more tissue ingrowth was observed with channeled scaffold A (30%), B (45%), and C (53%) in contrast to 5% of the non-channeled controls. In vivo implantation of any foreign objects would unavoidably induce the polarization of invaded macrophages, either iNOS-positive pro-inflammatory macrophages (M1) or CD206-positive anti-inflammatory macrophages (M2) [56–58]. After 4 weeks of implantation, immunofluorescence staining for these markers confirmed that CD206 and iNOS positive cells distributed throughout the microchannels of channeled scaffolds (Fig. 8D). In contrast, macrophages are mainly distributed around the peripheral boundary region of the non-channeled scaffolds. Image analysis further showed that the number of CD206-positive cells was significantly higher in channeled scaffolds than in non-channeled controls, whilst the number of iNOS-positive cells in channeled scaffolds was close to that in control scaffolds. These data suggested that channeled SF scaffolds had better immunomodulatory and biocompatible properties. By now, all the results demonstrate the superiority of channeled scaffolds in promoting tissue ingrowth via encouraging cellularization and vascularization through the interconnected microchannels.

Clearly, the use of 3D printed PEC structures as sacrificial templates to create arbitrary channels within a broad spectrum of materials represents a practical and innovative approach toward the development of 3D complex tissue-engineering scaffolds with well-controlled micro-and macro-structure while maintaining a high reproducibility.

4. Conclusions

Here, we develop a simple yet versatile strategy to create 3D hierarchical microchannel networks within various castable materials using the PEC structures as sacrificial templates. With the help of a customized 3D printer, the PEC sacrificial templates could be printed directly from PEC coacervate with tailorable architectures in a 25% Pluronic F127 bath. Several associated innovations can be identified with the optimized combination of PEC bioink and Pluronic F127 supporting matrix for EB3DP, including 1) the formation of complex and multilayer structures at a high printing resolution, 2) the relatively low barrier for scaleup, and 3) the strong error tolerance during fabrication. The hierarchical channel networks exhibited good patency in vitro and in vivo, promoted mass exchange to sustain high cell viability, and facilitated tissue regeneration and integration upon subcutaneous implantation. Such channeled scaffolds would greatly benefit the formation of physiologically relevant tissues as in vitro testing tissue models or for in vivo reconstructive surgery.

CRediT authorship contribution statement

Haoyu Wang: Conceptualization, Methodology, Software, Validation, Formal analysis, Investigation, Data curation, Writing – original draft, Writing – review & editing, Visualization. **Xiaqing Zhou:** Methodology, Software, Validation, Formal analysis, Writing – original draft, Visualization. **Juan Wang:** Investigation, Data curation, Resources. **Xinping Zhang:** Writing – review & editing. **Meifeng Zhu:** Conceptualization, Methodology, Resources, Writing – review & editing, Funding acquisition. **Hongjun Wang:** Conceptualization, Methodology, Resources, Writing – review & editing, Funding acquisition, Supervision.

Declaration of interests

The authors declare that they have no known competing financial interests or personal relationships that could have appeared to influence the work reported in this paper.

Acknowledgements

This study was financially supported by National Science Foundation (NSF-DMR award number 1508511) and NIAMS award number 1R01AR067859. The authors are also grateful for the technical support from Dr. Yuhao Wang (Stevens Institute of Technology).

Appendix A. Supplementary data

Supplementary data to this article can be found online at https://doi.org/10.1016/j.bioactmat.2022.01.030.

References

[1] S.J. Hollister, Scaffold design and manufacturing: from concept to clinic, Adv. Mater. 21 (2009) 3330–3342.
[2] E. Santos, R.M. Hernández, J.L. Pedraz, G. Orive, Novel advances in the design of three-dimensional bio-scaffolds to control cell fate: translation from 2D to 3D, Trends Biotechnol. 30 (2012) 331–341.
[3] S. Bose, M. Roy, A. Bandyopadhyay, Recent advances in bone tissue engineering scaffolds, Trends Biotechnol. 30 (2012) 546–554.
[4] W.L. Murphy, R.G. Dennis, J.L. Kileny, D.J. Mooney, Salt fusion: an approach to improve pore interconnectivity within tissue engineering scaffolds, Tissue Eng. 8 (2002) 43–52.
[5] S.S. Kim, M. Sun Park, O. Jeon, C. Yong Choi, B.S. Kim, Poly(lactide-co-glycolide)/hydroxyapatite composite scaffolds for bone tissue engineering, Biomaterials 27 (2006) 1399–1409.
[6] H.J. Chung, T.G. Park, Surface engineered and drug releasing pre-fabricated scaffolds for tissue engineering, Adv. Drug Deliv. Rev. 59 (2007) 249–262.
[7] J. Grenier, H. Duval, F. Barou, P. Lv, B. David, D. Letourneur, Mechanisms of pore formation in hydrogel scaffolds textured by freeze-drying, Acta Biomater. 94 (2019) 195–203.
[8] S.J. Hollister, Porous scaffold design for tissue engineering, Nat. Mater. 4 (2005) 518–524.
[9] J.K. Sherwood, S.L. Riley, R. Palazzolo, S.C. Brown, D.C. Monkhouse, M. Coates, et al., A three-dimensional osteochondral composite scaffold for articular cartilage repair, Biomaterials 23 (2002) 4739–4751.
[10] Skylar-Scott Mark A, Uzel Sebastien GM, Nam Lucy L, Ahrens John H, Truby Ryan L, Damaraju S, et al. Biomanufacturing of organ-specific tissues with high cellular density and embedded vascular channels. Sci. Adv..5:eaaw2459.
[11] K.S. Lim, M. Baptista, S. Moon, T.B.F. Woodfield, J. Rnjak-Kovacina, Microchannels in development, survival, and vascularisation of tissue analogues for regenerative medicine, Trends Biotechnol. 37 (2019) 1189–1201.
[12] C. Mandrycky, Z. Wang, K. Kim, D.H. Kim, 3D bioprinting for engineering complex tissues, Biotechnol. Adv. 34 (2016) 422–434.
[13] M.A. Heinrich, W. Liu, A. Jimenez, J. Yang, A. Akpek, X. Liu, et al., 3D bioprinting: from benches to translational applications, Small 15 (2019), e1805510.
[14] S. Vijayavenkataraman, W.C. Yan, W.F. Lu, C.H. Wang, J.Y.H. Fuh, 3D bioprinting of tissues and organs for regenerative medicine, Adv. Drug Deliv. Rev. 132 (2018) 296–332.
[15] J. Rouwkema, N.C. Rivron, C.A. van Blitterswijk, Vascularization in tissue engineering, Trends Biotechnol. 26 (2008) 434–441.
[16] L.R. Madden, D.J. Mortisen, E.M. Sussman, S.K. Dupras, J.A. Fugate, J.L. Cuy, et al., Proangiogenic scaffolds as functional templates for cardiac tissue engineering, Proc. Natl. Acad. Sci. U. S. A. 107 (2010) 15211–15216.
[17] Y. Cao, Y.F. Poon, J. Feng, S. Rayatpisheh, V. Chan, M.B. Chan-Park, Regulating orientation and phenotype of primary vascular smooth muscle cells by biodegradable films patterned with arrays of microchannels and discontinuous microwalls, Biomaterials 31 (2010) 6228–6238.
[18] S. Li, F. Tallia, A.A. Mohammed, M.M. Stevens, J.R. Jones, Scaffold channel size influences stem cell differentiation pathway in 3-D printed silica hybrid scaffolds for cartilage regeneration, Biomater. Sci. 8 (2020) 4458–4466.
[19] Y. Fang, T. Zhang, L. Zhang, W. Gong, W. Sun, Biomimetic design and fabrication of scaffolds integrating oriented micro-pores with branched channel networks for myocardial tissue engineering, Biofabrication 11 (2019), 035004.
[20] V.K. Lee, D.Y. Kim, H. Ngo, Y. Lee, L. Seo, S.S. Yoo, et al., Creating perfused functional vascular channels using 3D bio-printing technology, Biomaterials 35 (2014) 8092–8102.
[21] H.M. Eltaher, F.E. Abukunna, L. Ruiz-Cantu, Z. Stone, J. Yang, J.E. Dixon, Human-scale tissues with patterned vascular networks by additive manufacturing of sacrificial sugar-protein composites, Acta Biomater. 113 (2020) 339–349.
[22] M. Zhu, W. Li, X. Dong, X. Yuan, A.C. Midgley, H. Chang, et al., In vivo engineered extracellular matrix scaffolds with instructive niches for oriented tissue regeneration, Nat. Commun. 10 (2019) 4620.
[23] D.B. Kolesky, K.A. Homan, M.A. Skylar-Scott, J.A. Lewis, Three-dimensional bioprinting of thick vascularized tissues, Proc. Natl. Acad. Sci. U. S. A. 113 (2016) 3179–3184.
[24] J.S. Miller, K.R. Stevens, M.T. Yang, B.M. Baker, D.H. Nguyen, D.M. Cohen, et al., Rapid casting of patterned vascular networks for perfusable engineered three-dimensional tissues, Nat. Mater. 11 (2012) 768–774.
[25] R.L. Truby, J.A. Lewis, Printing soft matter in three dimensions, Nature 540 (2016) 371–378.
[26] T. Bhattacharjee, S.M. Zehnder, K.G. Rowe, S. Jain, R.M. Nixon, W.G. Sawyer, et al., Writing in the granular gel medium, Sci. Adv. 1 (2015), e1500655.
[27] A.K. Grosskopf, R.L. Truby, H. Kim, Viscoplastic matrix materials for embedded 3D printing, ACS Appl. Mater. Interfaces 10 (2018) 23353–23361.
[28] W. Wu, A. DeConinck, J.A. Lewis, Omnidirectional printing of 3D microvascular networks, Adv. Mater. 23 (2011) H178–H183.
[29] P. Schaaf, J.B. Schlenoff, Saloplastics: processing compact polyelectrolyte complexes, Adv. Mater. 27 (2015) 2420–2432.
[30] R. Basak, R. Bandyopadhyay, Encapsulation of hydrophobic drugs in pluronic F127 micelles: effects of drug hydrophobicity, solution temperature, and pH, Langmuir 29 (2013) 4350–4356.
[31] S-k Ahn, R.M. Kasi, S.-C. Kim, N. Sharma, Y. Zhou, Stimuli-responsive polymer gels, Soft Matter 4 (2008) 1151–1157.
[32] S. Edvinas, K. Sigita, J. Linas, O. Jolita, M. Mangirdas, Photosensitive naturally derived resins toward optical 3-D printing, Opt. Eng. 57 (2018) 1–9.
[33] P. Wang, Y. Sun, X. Shi, H. Shen, H. Ning, H. Liu, 3D printing of tissue engineering scaffolds: a focus on vascular regeneration, Bio-Design Manufac. 4 (2021) 344–378.
[34] X. Du, L. Wu, H. Yan, Z. Jiang, S. Li, W. Li, et al., Microchannelled alkylated chitosan sponge to treat noncompressible hemorrhages and facilitate wound healing, Nat. Commun. 12 (2021) 4733.
[35] H.J. Wang, M. Bertrand-De Haas, J. Riesle, E. Lamme, C.A. Van Blitterswijk, Tissue engineering of dermal substitutes based on porous PEGT/PBT copolymer scaffolds: comparison of culture conditions, J. Mater. Sci. Mater. Med. 14 (2003) 235–240.
[36] H.J. Wang, M. Bertrand-de Haas, C.A. van Blitterswijk, E.N. Lamme, Engineering of a dermal equivalent: seeding and culturing fibroblasts in PEGT/PBT copolymer scaffolds, Tissue Eng. 9 (2003) 909–917.
[37] J. Fu, H.M. Fares, J.B. Schlenoff, Ion-pairing strength in polyelectrolyte complexes, Macromolecules 50 (2017) 1066–1074.
[38] Q. Wang, J.B. Schlenoff, The polyelectrolyte complex/coacervate continuum, Macromolecules 47 (2014) 3108–3116.
[39] H.H. Hariri, J.B. Schlenoff, Saloplastic macroporous polyelectrolyte complexes: cartilage mimics, Macromolecules 43 (2010) 8656–8663.
[40] R.A. Ghostine, R.F. Shamoun, J.B. Schlenoff, Doping and diffusion in an extruded saloplastic polyelectrolyte complex, Macromolecules 46 (2013) 4089–4094.
[41] C.H. Porcel, J.B. Schlenoff, Compact polyelectrolyte complexes: "saloplastic" candidates for biomaterials, Biomacromolecules 10 (2009) 2968–2975.
[42] H.M. Fares, J.B. Schlenoff, Diffusion of sites versus polymers in polyelectrolyte complexes and multilayers, J. Am. Chem. Soc. 139 (2017) 14656–14667.
[43] R. Zhang, Y. Zhang, H.S. Antila, J.L. Lutkenhaus, Role of salt and water in the plasticization of PDAC/PSS polyelectrolyte assemblies, J. Phys. Chem. B 121 (2017) 322–333.
[44] K. Sadman, Versatile and high-throughput polyelectrolyte complex membranes via phase inversion, ACS Appl. Mater. Interfaces 11 (2019) 16018–16026.
[45] M. Bohorquez, C. Koch, T. Trygstad, N. Pandit, A study of the temperature-dependent micellization of pluronic F127, J. Colloid Interface Sci. 216 (1999) 34–40.
[46] Z. Jiang, B. Diggle, M.L. Tan, J. Viktorova, C.W. Bennett, L.A. Connal, Extrusion 3D printing of polymeric materials with advanced properties, Adv. Sci. 7 (2020) 2001379.
[47] L. Gao, C. Li, F. Chen, C. Liu, Fabrication and characterization of toughness-enhanced scaffolds comprising β-TCP/POC using the freeform fabrication system with micro-droplet jetting, Biomed. Mater. (Bristol, England) 10 (2015), 035009.
[48] J. Tang, J. Guo, Z. Li, C. Yang, D. Xie, J. Chen, et al., A fast degradable citrate-based bone scaffold promotes spinal fusion, J. Mater. Chem. B 3 (2015) 5569–5576.
[49] Y. Guo, R.T. Tran, D. Xie, Y. Wang, D.Y. Nguyen, E. Gerhard, et al., Citrate-based biphasic scaffolds for the repair of large segmental bone defects, J. Biomed. Mater. Res. 103 (2015) 772–781.
[50] H. Wang, C.A. van Blitterswijk, The role of three-dimensional polymeric scaffold configuration on the uniformity of connective tissue formation by adipose stromal cells, Biomaterials 31 (2010) 4322–4329.
[51] D.J. Mooney, A.G. Mikos, Growing new organs, Sci. Am. 280 (1999) 60–65.
[52] R.K. Jain, P. Au, J. Tam, D.G. Duda, D. Fukumura, Engineering vascularized tissue, Nat. Biotechnol. 23 (2005) 821–823.
[53] R.K. Jain, Transport of molecules, particles, and cells in solid tumors, Annu. Rev. Biomed. Eng. 1 (1999) 241–263.
[54] B.J. McGuire, T.W. Secomb, Estimation of capillary density in human skeletal muscle based on maximal oxygen consumption rates, Am. J. Physiol. Heart Circ. Physiol. 285 (2003) H2382–H2391.
[55] N. Koike, D. Fukumura, O. Gralla, P. Au, J.S. Schechner, R.K. Jain, Tissue engineering: creation of long-lasting blood vessels, Nature 428 (2004) 138–139.
[56] Y.T. Konttinen, J. Pajarinen, Y. Takakubo, J. Gallo, C. Nich, M. Takagi, et al., Macrophage polarization and activation in response to implant debris: influence by "particle disease" and "ion disease, J. Long Term Eff. Med. Implants 24 (2014) 267–281.
[57] E.M. Sussman, M.C. Halpin, J. Muster, R.T. Moon, B.D. Ratner, Porous implants modulate healing and induce shifts in local macrophage polarization in the foreign body reaction, Ann. Biomed. Eng. 42 (2014) 1508–1516.
[58] G.S.A. Boersema, N. Grotenhuis, Y. Bayon, J.F. Lange, Y.M. Bastiaansen-Jenniskens, The effect of biomaterials used for tissue regeneration purposes on polarization of macrophages, BioResearch Open Access 5 (2016) 6–14.